


Self-sustaining cycle of purely elastic turbulence

Jiaxing Song 

Department of Modern Mechanics, University of Science and Technology of China,
Hefei, Anhui 230026, China
and Max Planck Institute for Solar System Research, Göttingen, 37077, Germany

Fenghui Lin , Yabiao Zhu , Zhen-Hua Wan , Nansheng Liu ,* and Xi-Yun Lu 

Department of Modern Mechanics, University of Science and Technology of China,
Hefei, Anhui 230026, China

Bamin Khomami [†]

Department of Chemical and Biomolecular Engineering, University of Tennessee,
Knoxville, Tennessee 37996, USA



(Received 7 March 2022; accepted 20 December 2022; published 13 January 2023)

Direct numerical simulation of purely elastic turbulence (ET) in the Taylor-Couette flow of dilute polymer solutions is used to identify the dominant flow structures, namely, unsteady diwhirls that almost span the entire gap and axially and azimuthally elastic waves that occupy the inner rotating cylinder region to midgap. In accord with experiment, the azimuthal wave speed increases monotonically with enhanced Wi and it travels nearly 50 times faster than the axial waves. The interaction of elastic waves with unsteady diwhirls leads to stochastic or chaotic cycles of polymer stretch and relaxation and commensurate fluctuations in elastic stresses over a broad range of spatiotemporal frequency that produce turbulent kinetic energy and sustain turbulent dynamics. To this end, the self-sustaining cycle of ET is elucidated. Overall, this study paves the way for mechanistic understanding of this inertia less turbulence in curvilinear flows.

DOI: [10.1103/PhysRevFluids.8.014602](https://doi.org/10.1103/PhysRevFluids.8.014602)

I. INTRODUCTION

Turbulence is a ubiquitous phenomenon where the fluid motion exhibits a broad range of spatial and temporal scales. Turbulent flows typically manifest enhanced flow resistance and mixing when compared with their laminar flow counterparts. In Newtonian flows, turbulence is realized at high Reynolds number ($Re \gg 1$) where convective effects are dominant [1–3], however, in the flows of dilute polymeric solutions turbulence occurs even at very low $Re \ll 1$ when elastic forces become significant (Weissenberg number $Wi \gg 1$) [4–6]. In the former case, nonlinear inertial forces give rise to turbulence, whereas in the latter, nonlinear elastic stresses generated by polymer dynamics

*Ins@ustc.edu.cn

[†]bkhomami@utk.edu

Published by the American Physical Society under the terms of the [Creative Commons Attribution 4.0 International](https://creativecommons.org/licenses/by/4.0/) license. Further distribution of this work must maintain attribution to the author(s) and the published article's title, journal citation, and DOI. Open access publication funded by the Max Planck Society.

lead to a hierarchy of purely elastic instabilities that give rise to an inertia less purely elastic turbulence (ET) [5–11]. Unlike inertial turbulence that has been extensively studied for well over a century, ET in shear flows of dilute polymeric solutions was discovered only two decades ago [12].

Existence of purely elastic instability above a critical Wi and at negligible $Re \approx 10^{-3}$ has been experimentally observed in many flow geometries that are routinely used for rheological characterization of complex fluids, namely, the Taylor-Couette (TC), cone-and-plate and parallel plate flow geometries [10,12–18]. To that end, TC flow has served as a prototypical geometry for study of bifurcations and pattern formation in curvilinear flows of dilute polymeric solutions [19–24]. To date, it has conclusively been shown that a purely elastic instability in TC flow occurs due to the coupling of radial velocity fluctuations and finite hoop stresses that lead to amplification of radial velocity perturbations, and a banded vortex secondary flow pattern [19,20]. Moreover, axisymmetric and nonaxisymmetric stability analyses performed by Beris and coworkers have demonstrated that the most unstable mode is nonaxisymmetric and time dependent [25–27]. Moreover, the possible flow patterns after the onset of purely elastic instability are shown to be ribbons (standing waves) and spirals (traveling waves) [25,26]. In fact, many intriguing flow patterns, such as rotating standing waves, disordered oscillations, oscillatory strips and solitary vortex pairs or “diwhirls” have been shown to arise as a result of higher-order elastically driven flow transitions in viscoelastic TC flow [21,28,29]. This hierarchy of elastically driven flow transitions culminated in discovery of purely ET [12]. Overall, the experimental studies of ET have shown that the flow is essentially spatially smooth and temporally random and it exhibits a broad range of spatiotemporal scales with a steep power-law decay in the velocity power spectra at all spatial scales [5,30–32]. Recently, the similarity of deviatoric stresses in ET and magneto-hydrodynamics has been used to suggest that elastic waves observed experimentally in ET are similar to Alfvén waves in magneto-hydrodynamics. This analogy allows an approximation of the elastic wave speed as $c_{el} = [\text{trace}(\tau_{ij})/\rho]^{1/2}$, where τ_{ij} is the polymeric elastic stress. In addition, the predicted increase in wave speed as a function of Wi , is postulated to exhibit a power-law scaling of $Wi^{0.7}$ [33].

The lack of experimental techniques for direct and realtime measurement of elastic stresses that arise from interaction of macromolecules with dominant flow structures has prevented detailed mechanistic understanding of the self-sustaining cycle that gives rise to ET [5]. Although the enhanced flow resistance and the steep decay in the velocity energy spectra that are hallmarks of ET have been observed in two-dimensional direct numerical simulations (DNS) of viscoelastic Kolmogorov [8,9,11], and TC flows [34], significant quantitative differences exist between the simulation results and experimental observations. These discrepancies have been attributed to the approximate nature of the simulated flow, especially its two-dimensionality. Hence, three-dimensional (3D) DNS of ET can pave the way for unraveling the complete interactions of elastic waves with coherent flow structures.

Due to the “high- Wi problem,” 3D DNS of purely elastic flow ($Re \ll 1$) has remained a grand challenge problem for the research community engaged in developing first-principle models and simulations that can predict faithfully the complex spatiotemporal dynamics of polymeric flows [35–37]. In this study, we present the results of the 3D DNS of ET at $Re = 0.01$ in TC flow of polymeric solutions. Specifically, it is demonstrated that, by increasing Wi , the incipient purely elastic instability gradually leads to a chaotic flow composed of unsteady diwhirls that originate in the outer wall region and almost span the entire gap as well as axially and azimuthally traveling elastic wave flow patterns that populate the inner wall region and extend to half of the gap width. Moreover, the drag enhancement (DE) of flow and the steep power-law decay of velocity energy spectra are in good agreement with the seminal experimental study of Groisman and Steinberg [7,12]. More importantly, based on a detailed examination of interactions between elastic stresses, elastic waves and commensurate velocity fluctuations with broad spatiotemporal scales, the self-sustaining cycle of ET has been elucidated.

II. PROBLEM FORMULATION AND COMPUTATIONAL DETAILS

In the present study we have chosen $d = R_o - R_i$, $d/(\Omega R_i)$, ΩR_i , $\rho(\Omega R_i)^2$, and $\eta_p \Omega R_i/d$ as scales for length, time, velocity \mathbf{u} , pressure P , and polymer stress $\boldsymbol{\tau}$, respectively. R_i and R_o are the inner and outer cylinder radii, respectively; Ω denotes the inner cylinder angular velocity, and ρ the solution density. The polymer stress $\boldsymbol{\tau}$ is related to the conformation tensor \mathbf{C} through the finitely extensible nonlinear elastic Peterlin (FENE-P) model [38]. The dimensionless governing equations for the incompressible flow of FENE-P fluid are

$$\nabla \cdot \mathbf{u} = 0, \quad (1)$$

$$\frac{\partial \mathbf{u}}{\partial t} + \mathbf{u} \cdot \nabla \mathbf{u} = -\nabla P + \frac{\beta}{Re} \nabla^2 \mathbf{u} + \frac{1-\beta}{Re} \nabla \cdot \boldsymbol{\tau}, \quad (2)$$

$$\frac{\partial \mathbf{C}}{\partial t} + \mathbf{u} \cdot \nabla \mathbf{C} = \mathbf{C} \cdot \nabla \mathbf{u} + (\nabla \mathbf{u})^T \cdot \mathbf{C} - \boldsymbol{\tau}, \quad (3)$$

where $\boldsymbol{\tau} = [\frac{L^2-3}{L^2-\text{trace}(\mathbf{C})}\mathbf{C} - \mathbf{I}]/Wi$, L is the maximum chain extensibility, $Re = \rho \Omega R_i d / \eta_t$ with the total zero-shear viscosity η_t being the sum of the solvent (η_s) and polymeric (η_p) contributions, $Wi = \lambda \Omega R_i / d$, where λ denotes the polymer relaxation time and the viscosity ratio $\beta = \eta_s / \eta_t$.

In this study we have used a proven pseudospectral finite-difference hybrid method [39] to simulate viscoelastic TC flow. Specifically, in the hybrid method technique, the convective term in the conformation tensor evolution equation is discretized with a second-order conservative total variation diminishing finite difference scheme with the MINMOD limiter [40]; the pseudospectral method discretization is used for all other terms, which maximally preserves accuracy and efficiency. The MINMOD limiter automatically converts the second-order finite-difference scheme to a first-order upwind scheme to suppress numerical oscillations caused by sharp gradients of \mathbf{C} . To strictly enforce the chain finite maximum extension limit, the time integration of the conformation tensor equation is performed by a semi-implicit second-order predictor-corrector Adams-Bashforth scheme [41–43], where the linear stress relaxation term is treated implicitly [44,45]. As expected this algorithm is numerically stable and preserves the symmetric-positive-definite (SPD) nature as well as the boundedness of the polymer conformation tensor ($0 < \text{trace}(\mathbf{C}) < L^2$). For more details about accuracy and validation of this code, the reader is referred to one of our previous papers [46]. It should be noted that in the study of homogeneous, isotropic turbulence with polymer additives, Perlekar and coworkers [47,48] also used a hybrid code, namely, a spectral method for solving the Navier-Stokes equation and a finite difference method for the FENE-P constitutive equation. Specifically, to preserve the SPD nature of \mathbf{C} , they used the Cholesky-decomposition scheme proposed by Vaithianathan *et al.* [44]. Moreover, in order to avoid dispersion errors caused by the sharp gradients of \mathbf{C} , they adapted the Kurganov-Tadmor shock-capturing scheme for the polymer-advection term [49,50]. An explicit fourth-order or sixth-order central-finite-difference scheme was used for other terms. Finally, to avoid numerical instability, i.e., ensure that $\text{trace}(\mathbf{C})$ remains smaller than L^2 , the second-order Adams-Bashforth time scheme with very small time steps were used.

Motivated by our recent DNS study of elasticity-dominated turbulence in TC flows [46,51], ET is realized by increasing the Wi from 0 to 120 at $Re = 0.01$ in a large-curvature TC geometry with $\eta = R_i/R_o = 0.5$. To avoid shear thinning effects, we have chosen $\beta = 0.9$ and $L = 100$. Based on our previous calculations [46,52], a large mesh size of $128 \times 128 \times 256$ for $Wi \leq 30$ and $128 \times 256 \times 512$ for $Wi \geq 60$ in the $r \times \theta \times z$ directions has been chosen to reliably capture the velocity and polymer stress fields at the relevant scales. Gauss-Lobatto-Chebyshev polynomials are used in the wall normal (r) direction and Fourier series in the periodic (θ and z) directions; grid points are clustered near the inner and outer walls in the r direction, and uniform in the θ and z directions. The de-aliasing cutoff is not used in the pseudospectral discretization [53]. The initial velocity and conformation fields are the Newtonian base flow and a unit tensor, respectively. A random perturbation of small amplitude, usually 0.0005 is added to the initial velocity and conformation

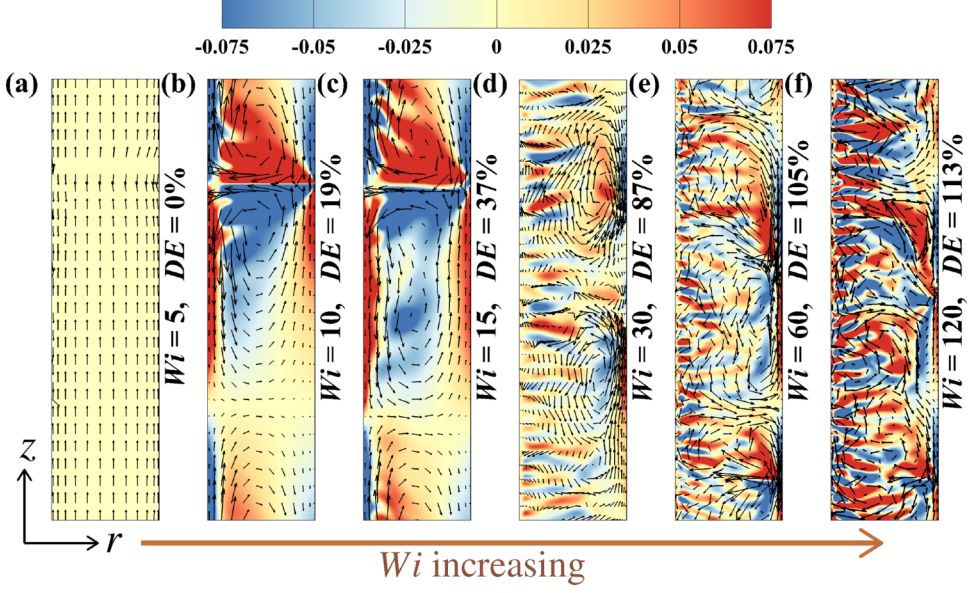


FIG. 1. Time and θ direction averaged vectors of radial ($\langle u_r \rangle_{\theta,t}$) and axial ($\langle u_z \rangle_{\theta,t}$) velocities and contour plots of streamwise vorticity $\langle \omega_\theta \rangle_{\theta,t}$ in (r, z) plane for various Wi at $Re = 0.01$ with $0 \leq z \leq \pi d$ and $R_i \leq r \leq R_o$. DE is calculated as the increased angular momentum to the laminar value.

fields to accelerate flow destabilization. As Wi is progressively increased the converged numerical results at a smaller Wi are used as the initial flow field. It should be noted that, in very-low- Re simulations, the discretizations of viscous terms (the viscous and polymeric stresses divergence terms) are very large as compared with other terms in the momentum equation. To balance all the terms and avoid numerical errors during the calculation of velocities, a very small time step is needed to multiplied the viscous terms. This has already been demonstrated in the simulation of ET of von Kármán swirling flow, where Buel and Stark [54] proposed that when the momentum equations are solved by the time-integrated scheme, the numerical time step has to be smaller than the vorticity diffusion timescale, i.e., $\Delta t_v \leq t_v = \rho r^2 / \eta_s = Re_v / \Omega$, where $Re_v = \rho \Omega r^2 / \eta_s$, ρ is the density, η_s is solvent shear viscosity, Ω is the rotating angular velocity, and r is the radius of the plate. To that end, at a given $Wi_v = \lambda \Omega r / d$, where λ is the characteristic relaxation time of polymers and d is the gap width between two plates, the vorticity diffusion timescale is given by $t_v = Re_v \lambda r / (Wi_v d)$. Evidently, the time step depends on both Re_v and Wi_v ; hence, the combination of smallest Re_v and largest Wi_v requires the smallest time step. In the numerical calculation, Wi should be defined by the local characteristic shear rate. Generally, in the low- Re ($Re \ll 1$) simulation, the actual time step should be approximately $\Delta t \leq t_v \sim Re / Wi$. Hence in the present simulations with $Re = 0.01$, $Wi \approx 100$, the small time step of $\Delta t \approx 0.0001$ is used. Sufficiently long simulations (typically of $\approx 20\lambda$) are executed to ensure that the statistically stationary flow states have been realized. Moreover, ensemble averages are obtained over a time period of $\approx 10\lambda$. The governing equations are supplemented by no-slip boundary conditions at the walls, as well as periodic boundary conditions in the z direction. The values of the conformation tensor at the walls are directly evaluated from the integration of the constitutive equation at the solid boundaries [41,55,56].

III. RESULTS AND DISCUSSIONS

In the limit of vanishing inertia, as Wi surpasses a critical value of $Wi_c \approx 10$, the azimuthal Couette flow depicted in Fig. 1(a) becomes unstable and a large-scale banded vortex secondary

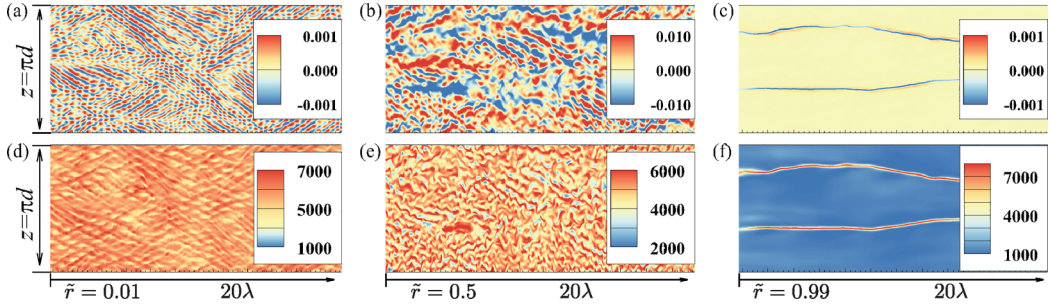


FIG. 2. (a)–(c) Axial space-time plots of radial velocity u_r and (d)–(f) polymer chain extension trace(\mathbf{C}) obtained along an axial line near the inner wall ($\tilde{r} = 0.01$) showing the traveling waves-like flow patterns; at the middle gap ($\tilde{r} = 0.5$) the disordered oscillations, and near the outer wall ($\tilde{r} = 0.99$) diwhirls, respectively, with $\theta = \pi$ for ET at $Re = 0.01$, $Wi = 30$. Hereafter, $\tilde{r} = (r - R_i)/d$ is the dimensionless distance to the inner cylinder wall.

flow is realized. In concert with experimental observation, the increase in Wi leads to higher-order flow transitions and eventual appearance of solitary vortex pairs or diwhirls [see Figs. 1(b)–1(c)] [28,29,57]. Further increase in Wi leads to a “chaotic” flow, especially near the inner cylinder and the ET flow state is attained at $Wi \geq 30$ [see Figs. 1(d)–1(f)]. Specifically, in the ET flow state, in addition to the two pairs of unsteady diwhirls that nearly span the entire gap, numerous small-scale streamwise vortices populate the inner cylinder wall region. As shown earlier, these small-scale streamwise vortices are elastic Görtler vortices [46,58]. Surprisingly, these vortices are wrapped up on the inner half side of the diwhirls much like high- Re inertial Görtler vortices formed over the convex inner wall that are nested with large-scale Taylor vortices [59]. This similarity is intriguing due to the fact that the driving mechanism for formation of the dominant flow structures in ET, namely, diwhirls and elastic Görtler vortices, arise as Wi is progressively increased above a critical value in absence of inertia. Finally, a commensurate monotonic increase in DE is observed with increasing Wi (see Fig. 1). The maximum DE, namely, 113% is obtained at $Wi = 120$, which is much smaller than the 4 times flow resistance (in comparison with the corresponding laminar flow) at $Wi \approx 40$ observed in the original experiments [12]. However, it should be noted that lack of detailed characterization of the experimental fluid used in the experiments [12] precludes a one-to-one comparison of experimental and simulation findings.

The turbulent flow that is realized as a result of a sequence of hoop-stress driven flow transitions, namely, ET, exhibits complex spatiotemporal dynamics with a strong radial dependence (see Figs. 2 and 3). Specifically, near the inner cylinder wall [see Fig. 2(a)], in addition to localized rotating standing waves also known as ribbons, traveling-wave-like patterns are observed. It is well known that ribbons arise due to superposition of an upward and downward spiral traveling wave of the same amplitude [28,53,60]. In the ET flow state these waves have slightly different amplitudes much alike the disordered oscillations seen in experiments [28]. These disordered oscillations are nonaxisymmetric, as evinced by the distinct traveling-wave patterns in azimuthal space-time plots (see Fig. 3). At the middle of the gap axially traveling-wave-like flow patterns are hard to discern since the flow is essentially a spatiotemporally chaotic flow [see Fig. 2(b)]. However, from the middle of the gap to surface of the rotating inner cylinder the azimuthal and axial traveling-wave patterns are the dominant flow structures [see Figs. 3(a) and 3(b)]. The region near the outer cylinder is mainly occupied by unsteady diwhirls and it is devoid of axially and azimuthally traveling waves; hence, intense localized inflows and spatiotemporally unsteady oscillations are observed [see Figs. 2(c) and 2(f)]. The corresponding polymer chain stretch quantified via trace(\mathbf{C}) in different radial positions is shown in Figs. 2(d)–2(f) and 3(d)–3(f). As expected, trace(\mathbf{C}) exhibits patterns that are consistent with the corresponding velocities along the specific spatial lines. For example, along a given axial line in the axial space-time plot of Figs. 2(c) and 2(f) the patterns of trace(\mathbf{C}) are

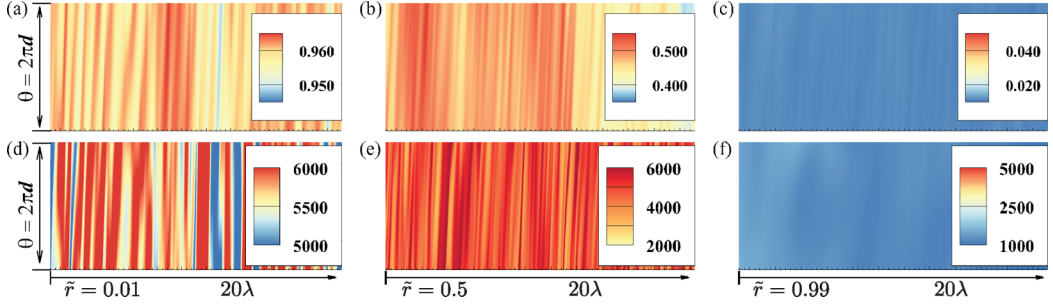


FIG. 3. (a)–(c) Azimuthal space-time plots of azimuthal velocity u_θ and (d)–(f) polymer chain extension trace(C) obtained along an azimuthal line near the inner wall ($\tilde{r} = 0.01$) showing the traveling-wave-like flow patterns; at the middle gap ($\tilde{r} = 0.5$) the traveling-wave-like flow patterns, and near the outer wall ($\tilde{r} = 0.99$) there is no obvious traveling-wave-like flow patterns, respectively, with $z = \pi d/2$ for ET at $Re = 0.01$, $Wi = 30$.

consistent with that of the radial velocity u_r . Evidently, the intense extensionally dominant radial inflow induced by large-scale diwhirls readily stretch polymers and a commensurately high value of trace(C) is attained. Consequently, the polymer chains are highly stretched in the two localized extensional inflows associated with the diwhirls in the outer wall region. While in the inner-half gap regions of Figs. 2(a), 2(b) and 2(d), 2(e), the polymer chains exhibit temporal and spatial oscillations over a broad spatiotemporal scale due to rapid stretching and relaxation events induced by the flow. This in turn leads to significant fluctuation of elastic stresses τ' that sustains ET dynamics.

To accurately determine the speed of traveling elastic waves, temporal cross correlations of velocity of two spatially separated points (Δx) are calculated at various Wi . The elastic wave speed in turn can be calculated as the ratio of spatially separated points (Δx) and the shifted lag time (τ_{lag}) [33,61]. Specifically, a temporal cross-correlation function $C_{u_r}(\Delta x, \tau)$ of radial velocity u_r is given as

$$C_{u_r}(\Delta x, \tau) = \frac{\langle u_r(x, t)u_r(x + \Delta x, t + \tau) \rangle}{\langle u_r(x, t)u_r(x + \Delta x, t) \rangle}. \quad (4)$$

The streamwise (azimuthal) elastic waves, as depicted in Figs. 3(a), 3(b), 3(d), 3(e) only occur in the inner half of the gap. The temporal cross-correlation function at various separation distance show a positive shift peak with a lag time τ_{lag} at the vicinity of $\tau_l = 0$ [see Fig. 4(a)]. This indicates that the azimuthal elastic wave propagates in a given direction with increasing $\Delta\theta$. Note

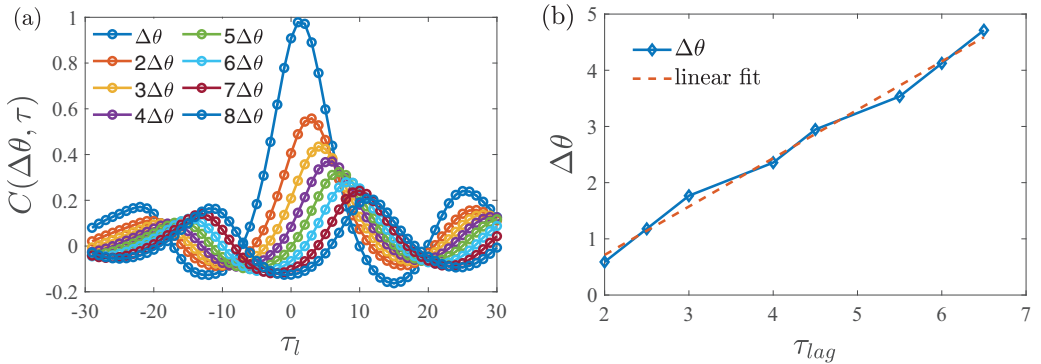


FIG. 4. (a) Azimuthal temporal cross-correlation function of radial velocity $C(\Delta\theta, \tau)$ versus lag time τ_l for different $\Delta\theta$ at middle gap for $Wi = 30$ with $Re = 0.01$. The separation distance $\Delta\theta = (R_i + R_o)\pi/16$. (b) The separation distance $\Delta\theta$ versus shift lag time τ_{lag} and the corresponding linear fit.

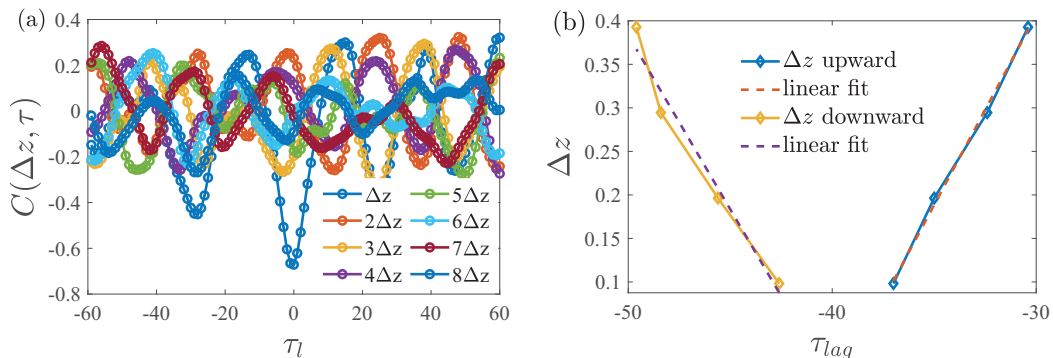


FIG. 5. (a) Axial temporal cross-correlation function of radial velocity $C(\Delta z, \tau)$ versus lag time τ_l for different values Δz at middle gap for $Wi = 30$ with $Re = 0.01$. The separation distance $\Delta z = \pi d/32$. (b) The separation distance Δz versus shift lag time τ_{lag} and a linear fit to it for both upward and downward waves.

that a perfect correlation and anticorrelation correspond to $C(\Delta\theta, \tau) = 1$ and $C(\Delta\theta, \tau) = -1$, respectively, while an uncorrelated signal has $C(\Delta\theta, \tau) = 0$. At $Wi < 15$, a distinct peak in the temporal cross-correlation function is not detected even for a very small separation distance of $\Delta\theta_s = (R_i + R_o)\pi/128$. This suggests azimuthal elastic waves first appear at $Wi = 15$. If the wave speed is constant, then there will be a linear relationship between $\Delta\theta$ and τ_{lag} . As expected, in Fig. 4(b), $\Delta\theta$ depicts a monotonic increase with τ_{lag} . Following the same procedure used by Varshney and Steinberg [33], we use the slope of the linear fit of $\Delta\theta$ versus τ_{lag} to determine the wave speed, which equals 0.4305. It should be noted that the wave speed obtained by the linear fit of the data is independent of the minimum separation distance $\Delta\theta$. However, given the finite wave speed, in order to get a clear temporal cross correlation, the time for propagation of the wave across a given distance $\Delta\theta$ should be small compared with the elastic relaxation timescale (λ) but large enough to minimize the sampling time interval, i.e., $d/(\Omega R_i)$ in this study.

Axial elastic waves are first observed at $Wi = 30$. As depicted in Fig. 5(a), in the vicinity of $\tau_l = 0$, the axial temporal cross-correlation function $C(\Delta z, \tau)$ with various separation distances Δz exhibits both positive and negative shift peak lag times τ_{lag} . This behavior is attributed to the existence of upward and downward propagating axial elastic waves. As a consequence, the temporal cross-correlation function almost displays an axisymmetric distribution along $\tau_l = 0$. Therefore, it is not straightforward to determine the continuous peak shift of the lag time τ_{lag} with increasing Δz . Here, we can only get the first four separated distances with their shift lag time with both upward (positive shift lag time) and downward (negative shift lag time) elastic waves. As depicted in Fig. 5(b), the best linear fit of the data determines an upward axial elastic wave speed of 0.0087, and a downward axial elastic wave speed of -0.0080 , respectively. The upward and downward elastic wave speeds are nearly equal but have opposite directions. This is consistent with the axial space-time plots in Figs. 2(a) and 2(d). The azimuthal wave speed is about 50 times larger than the axial wave speed. It should be noted that, in order to accurately determine the small axial elastic wave speed, a corresponding narrower separate distance as well as longer sampling time should be used as compared with the azimuthal direction. As discussed above, the axial wave speed is much smaller than the azimuthal wave and the complicated temporal cross-correlation function precludes its accurate characterization. To that end, the azimuthal temporal cross-correlations of radial velocity of two spatially separated points are calculated at various Wi to determine the relationship between dominated azimuthal wave speed and fluid elasticity. As demonstrated in Fig. 6(a), in accord with experimental findings the elastic wave speed increases as Wi is enhanced. Despite the limited number of data points, the experimentally observed scaling of $Wi^{0.7}$ is observed with 98% confidence [33].

Elastic waves have been proposed to play a central role in the transfer of elastic energy to turbulent kinetic energy (TKE), albeit the precise mechanism by which this transfer occurs is

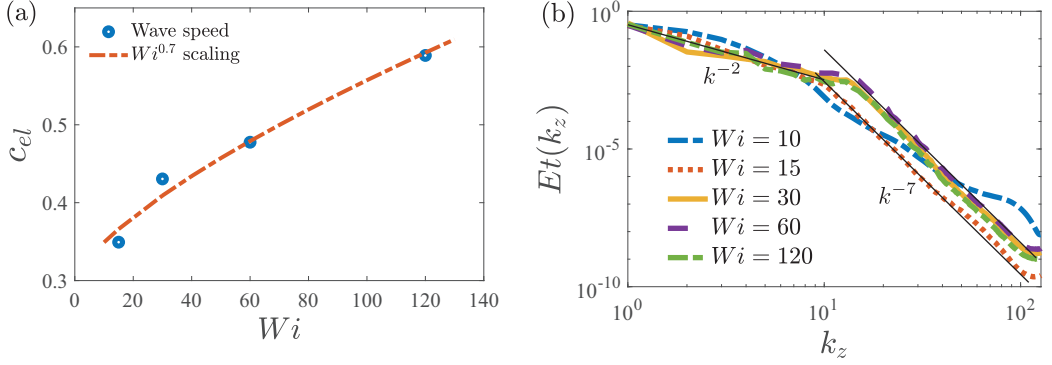


FIG. 6. (a) Azimuthal (streamwise) elastic wave speed for $Wi \geq 15$ at the middle gap. The red dashed line represents the best fit of $0.01Wi^{0.7} + 0.3$ with 98% confidence, i.e., the exponent obtained by Varshney and Steinberg [33]. (b) One-dimensional spanwise spectra of the TKE $(\langle u' \cdot u' \rangle / 2)$ normalized by its streamwise component $(\langle u'_\theta u'_\theta \rangle / 2)$ sampled at the middle of the gap for various Wi . Here the scaling exponent of k^{-2} at low-wave-number range is a guide for eye. In the present study, $\langle \rangle = \langle \langle \langle \rangle_\theta \rangle_z \rangle_t$ denotes hereinafter averaging in the θ direction, z direction and time, and the fluctuating part of variable v is obtained as $v' = v - \langle v \rangle$.

not yet understood [30]. However, Fouxon and Lebedev [30] have shown theoretically that, when elastic waves are present, the TKE spectra have to decay faster than k^{-3} , where k is the spatial wave number. This assertion is supported by our simulation results, namely, above $Wi = 10$ where elastic waves first appear, the TKE spectra show a continuous broad decay regime [see Fig. 6(b)]. Specifically, the energy spectra decay with a power-law exponent of approximately -2 at low wave numbers and approximately -7 at high wave numbers [see Fig. 6(b)]. Experimental measurements of the radial velocity power spectrum exhibits two contiguous regions of power-law decay with exponents of -1.1 and -2.2 in the low- and high-frequency regions, respectively [12]. Strikingly, at $Re = 10$, $Wi = 50$, these two power-law-decaying spectra of radial velocity were reproduced by Liu and Khomami via DNS of viscoelastic TC flow with the FENE-P constitutive model [62]. However, these simulations were performed in the elastically dominated flow regime in the presence of finite fluid-inertia dominated inner-wall region. In addition, in the oscillatory strips regime at $Wi = 30$, $Re = 90$, DNS studies of Khomami and coworkers [53] depict a broad spectra with two steep power-law-decay regions with exponents -2.4 at low frequencies and -5.54 at high frequencies. However, quantitative understanding of the relation between the present spectra and the corresponding experimentally measured spectra (in the frequency domain) remains an open question. Evidently, a detailed examination of the mechanism by which TKE is produced in ET can provide invaluable insight in this regard.

The absence of Reynolds shear stress $(\langle u'_r u'_\theta \rangle)$ in ET indicates that the TKE cannot be generated by the typical shear production term $(\langle u'_r u'_\theta \rangle \partial_r \langle u_\theta \rangle)$ seen in inertial turbulence [1–3]; hence, it has to be solely produced by the transformation of stored elastic potential energy [EPE, $E_p = (1 - \beta)(L^2 - 3)(\ln(f(\mathbf{C}))) / 2(Re Wi)$] in stretched polymers [63]. To exam the energy exchange process in ET, we recall the energy-budget equations. For viscoelastic turbulent flow, the budget equation for the mean kinetic energy (MKE) $E_m = U^2/2$ is given by

$$\frac{\partial E_m}{\partial t} + \mathbf{U} \cdot \nabla E_m = \nabla \cdot \left(\underbrace{-PU}_{D_{mp}} + \underbrace{2v_s \mathbf{U} \cdot \mathbf{S}}_{D_{ms}} + \underbrace{v_p \mathbf{U} \cdot \mathbf{T}}_{D_{me}} - \underbrace{\langle \mathbf{u}' \mathbf{u}' \rangle \cdot \mathbf{U}}_{D_{mt}} \right) - \underbrace{2v_s (\nabla \mathbf{U}) : \mathbf{S}}_{\varepsilon_m} - \underbrace{v_p (\nabla \mathbf{U}) : \mathbf{T}}_{P_{me}} + \underbrace{\langle \mathbf{u}' \mathbf{u}' \rangle : (\nabla \mathbf{U})}_{P_t}, \quad (5)$$

and for the TKE ($E_t = \langle \mathbf{u}' \cdot \mathbf{u}' \rangle / 2$)

$$\frac{\partial E_t}{\partial t} + \mathbf{U} \cdot \nabla E_t = \nabla \cdot \left(\underbrace{-\langle \mathbf{P}' \mathbf{u}' \rangle}_{D_p} + \underbrace{2v_s \langle \mathbf{u}' \cdot \mathbf{s}' \rangle}_{D_s} + \underbrace{v_p \langle \mathbf{u}' \cdot \boldsymbol{\tau}' \rangle}_{D_e} - \underbrace{\langle \mathbf{u}' \mathbf{u}' \cdot \mathbf{u}' \rangle / 2}_{D_t} \right) - \underbrace{2v_s \langle \mathbf{s}' : \mathbf{s}' \rangle}_{\varepsilon} - \underbrace{v_p \langle \mathbf{s}' : \boldsymbol{\tau}' \rangle}_{P_e} - \underbrace{\langle \mathbf{u}' \mathbf{u}' \rangle : (\nabla \mathbf{U})}_{P_t}, \quad (6)$$

and the budget equation for polymer additives EPE E_p

$$\frac{\partial E_p}{\partial t} + \mathbf{U} \cdot \nabla E_p = \underbrace{v_p \langle \mathbf{S} : \mathbf{T} \rangle}_{P_{me}} + \underbrace{v_p \langle \mathbf{s}' : \boldsymbol{\tau}' \rangle}_{P_e} - \underbrace{\frac{v_p}{2Wi} f(\langle \mathbf{C} \rangle) \text{trace}(\mathbf{T})}_{\varepsilon_{pm}} - \underbrace{\frac{v_p}{2Wi} \langle f(\mathbf{C}') \text{trace}(\boldsymbol{\tau}') \rangle}_{\varepsilon_{pt}}, \quad (7)$$

where $\mathbf{S} = (\nabla \mathbf{U} + (\nabla \mathbf{U})^T) / 2$, $\mathbf{s}' = (\nabla \mathbf{u}' + (\nabla \mathbf{u}')^T) / 2$ and $\mathbf{T} = \langle \boldsymbol{\tau} \rangle$, respectively. Specifically, in Eqs. (5)–(7), the left side represents the total time derivative of E_m , E_t , and E_p following a mean-flow fluid particle, while the right-hand side represents the various mechanisms that bring about changes to these quantities. The first four-divergence terms on right side of Eqs. (5) and (6) are energy transport and redistribution caused by pressure (D_{mp} , D_p), viscous diffusion (D_{ms} , D_s), polymeric elastic stress (D_{me} , D_e), and turbulent stress (D_{mt} , D_t), respectively. When integrated over the entire gap, these terms make no contributions to the total budget. The fifth term represents the direct viscous dissipation of kinetic energy (ε_m , ε) via its conversion into heat. It is important to emphasize that the sixth term represents the energy production associated with polymer stretch, which has been used to quantify energy conversion between kinetic energy and elastic energy, denoted as P_{me} and P_e respectively. And the last term is turbulence shear production term P_t that arises due to interaction of the mean streamwise velocity gradient and Reynolds shear stress. Here, P_t quantifies the loss of MKE in Eq. (5), but the gain of TKE in Eq. (6) [46]. In the EPE budget (Eq. (7)), the first two terms on right-hand side are the polymer energy production induced by mean P_{me} and fluctuations of elastic stress work P_e , respectively; whereas the last two terms are dissipation terms associated with the mean (ε_{pm}) and fluctuating (ε_{pt}) polymer chain motions [63,64].

A detailed TKE budget analysis clearly reveals that, in the ET flow state, TKE in TC flow is solely produced by the fluctuating elastic stress work term P_e [64]. Specifically, in the inner half of the gap [see Fig. 7(a)] the elastic production term gradually increases with Wi . After the onset of ET at $Wi = 30$, an intriguing change in P_e is observed, namely, its radial distribution, becomes positive nearly in the entire inner-wall region. The underlying TKE generation mechanism can be further scrutinized by a decomposition of P_e into its extension (P_e^e) and shear (P_e^s) components [see Fig. 7(b)]. The decomposition of the elastic product term into its extensional and shear parts is inspired by Steinberg [32], where the elastic stress is decomposed into its divergent and rotational or vortical parts. Note that P_e^e (P_e^s) corresponds to the work done by the divergent (rotational) component of fluctuating elastic stress via the fluctuating extensional (shear) flows. As seen in Fig. 7(b), before the onset of ET at $Wi = 15$, the production term is dominated by P_e^s ; after ET sets in at $Wi = 30$, P_e is dominated by P_e^e . This clearly indicates that the ET is essentially a turbulent flow state that results from significant coupling of polymer stretch and relaxation cycles and the fluctuating extensional flows. Specifically, the divergent part of fluctuating elastic stress associated with polymer stretch and relaxation cycles that mainly arise due to unsteady diwhirls give rise to TKE via elastic waves in the ET flow state.

Based on these findings the self-sustaining mechanism of ET in TC flow has three essential components. Specifically, as depicted in Fig. 8, (i) a purely elastic instability gives rise to steady

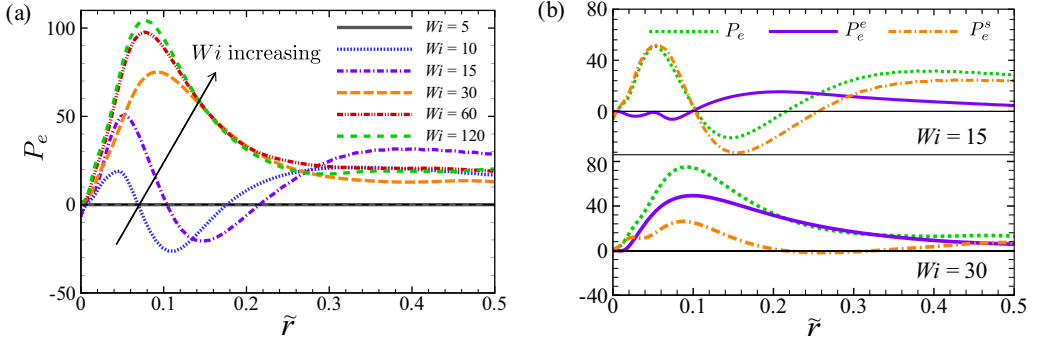


FIG. 7. (a) The elastic generation term $P_e = -(1 - \beta)\langle \boldsymbol{\tau}' : \boldsymbol{s}' \rangle / Re$ of the TKE, and (b) its extension [$P_e^e = -(1 - \beta)(\tau'_{rr}s'_{rr} + \tau'_{\theta\theta}s'_{\theta\theta} + \tau'_{zz}s'_{zz}) / Re$] and shear [$P_e^s = -2(1 - \beta)(\tau'_{r\theta}s'_{r\theta} + \tau'_{\theta z}s'_{\theta z} + \tau'_{rz}s'_{rz}) / Re$] parts at the inner half gap for $Wi = 15$ and $Wi = 30$.

diwhirls that in turn become unsteady due to flow perturbations (see iii); the unsteady intense inflows and commensurate high polymer stretch induced by diwhirls lead to a stochastic and chaotic polymer stretch and relaxation cycles that create elastic waves and commensurate large-scale fluctuations of the polymer stresses in the inner wall region ($\boldsymbol{\tau}'$). At the same time, small-scale fluid motions are generated along with a fluctuating strain rate (\boldsymbol{s}') due to the propagation of elastic waves, and (ii) the interaction of the fluctuating normal polymer stresses and fluctuating elongational strain give rise to TKE. Finally, (iii) the coupling of elastic waves near the inner wall and the resulting random velocity fluctuations destabilize the diwhirls. Hence, ET is sustained through these three components. Evidently, the flow is maintained by the external angular momentum input through the constant rotation of the inner cylinder. Thus, the self-sustaining mechanism described above is not the mechanism by which the flow is driven, rather it describes the mechanism that sustains the turbulence dynamics that arise via the interactions between coherent flow structures, elastic waves and fluctuating velocities in a flow that is essentially devoid of fluid inertia.

Finally, since the onset of ET coincides with appearance of axial waves at $Wi \geq 30$, one can postulate that the highly stretched polymers that are fed into the inner wall region at various diwhirl burst frequencies can easily be moved up and down the inner rotating walls by the axial or a combination axial and tilted azimuthal waves. This in turn leads to presence of highly stretched polymers in the near wall region with a relatively high shear rate. So, once these highly stretch chains with broad spatiotemporal scales enter the slow radial backflow toward the outer wall, they first

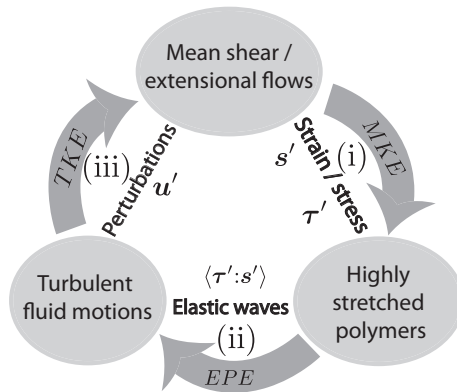


FIG. 8. Schematic depiction of the self-sustaining mechanism of ET.

rapidly collapse and then begin to go through cycles of stretch and relaxation due to the fluctuating strain in this region and finally collapse near the outer wall. This mechanism for the stochastic stretch and relaxation cycle of the polymers is “in a way” the axial analog of the mechanism for onset of purely elastic instability in TC flow, namely, coupling of radial velocity perturbations and hoop stresses that arise due to stretched polymers along a curved streamline. Here the perturbations are introduced by axial and potentially tilted azimuthal waves. To verify this postulate, one needs to compute several timescales, including the dominant frequencies of diwhirls, azimuthal and axial traveling waves, and the slow radial backflow. Clearly, in this strongly nonlinear turbulent flow, pressure, velocities and stresses and their corresponding timescales are correlated. To that end, to ascertain the validity of the above postulate, one needs to decompose the coherent structures to extract the dominant timescales and their interactions. This is well beyond the scope of this work. However, this issue will be addressed in our further study.

IV. CONCLUSIONS

To conclude, 3D DNS of ET in TC flow of dilute polymeric solutions has been realized. It is shown that the main flow features in ET are those of large-scale vortex pairs (unsteady diwhirls) and axial and azimuthal elastic waves. The large-scale vortex pairs and elastic waves dominate the outer and inner halves of the gap, respectively. Furthermore, turbulent velocity fluctuations of ET are mainly generated by the extensional part of polymer stress work ($\langle \tau' : s' \rangle$), which is associated with “stochastic” polymer stretch and relaxation cycles. The elastic waves induced by the highly stretched polymers are demonstrated to play a central role in generation of turbulent velocity fluctuations and the spectral property of the flow. These findings taken together have enabled the elucidation of the self-sustaining cycle of purely ET, thus paving the way for detailed understanding of elastic waves and flow physics in a host of low- Re turbulent flows of complex fluids.

ACKNOWLEDGMENTS

The authors would like to thank Xiaojue Zhu for useful discussions. This work was supported by the NSFC Grants No. 12172353, No. 11621202, No. 92052301, No. 92252202, and No. 11572312, Science Challenge Project (Grant No. TZ2016001), NSF Grant No. CBET0755269, and the Supercomputing Center of USTC. Jiaying Song acknowledges financial support from the Alexander von Humboldt Research Fellowship Foundation.

-
- [1] S. Grossmann, The onset of shear flow turbulence, *Rev. Mod. Phys.* **72**, 603 (2000).
 - [2] B. J. M. A. J. Smits and I. Marusic, High-Reynolds number wall turbulence, *Annu. Rev. Fluid Mech.* **43**, 353 (2011).
 - [3] J. Jiménez, Cascades in wall-bounded turbulence, *Annu. Rev. Fluid Mech.* **44**, 27 (2012).
 - [4] A. N. Morozov and W. van Saarloos, An introductory essay on subcritical instabilities and the transition to turbulence in visco-elastic parallel shear flows, *Phys. Rep.* **447**, 112 (2007).
 - [5] V. Steinberg, Elastic turbulence: An experimental view on inertialess random flow, *Annu. Rev. Fluid Mech.* **53**, 27 (2021).
 - [6] S. S. Datta, A. M. Ardekani, P. E. Arratia, A. N. Beris, I. Bischofberger, G. H. McKinley, J. G. Eggers, J. E. Lopez-Aguilar, S. M. Fielding, A. Frishman *et al.*, Perspectives on viscoelastic flow instabilities and elastic turbulence, *Phys. Rev. Fluids* **7**, 080701 (2022).
 - [7] A. Groisman and V. Steinberg, Elastic turbulence in a polymer solution flow, *Nature (London)* **405**, 53 (2000).
 - [8] S. Berti, A. Bistagnino, G. Boffetta, A. Celani, and S. Musacchio, Two-dimensional elastic turbulence, *Phys. Rev. E* **77**, 055306(R) (2008).

- [9] S. Berti and G. Boffetta, Elastic waves and transition to elastic turbulence in a two-dimensional viscoelastic Kolmogorov flow, *Phys. Rev. E* **82**, 036314 (2010).
- [10] L. Pan, A. Morozov, C. Wagner, and P. E. Arratia, Nonlinear Elastic Instability in Channel Flows at Low Reynolds Numbers, *Phys. Rev. Lett.* **110**, 174502 (2013).
- [11] H. Garg, E. Calzavarini, and S. Berti, Statistical properties of two-dimensional elastic turbulence, *Phys. Rev. E* **104**, 035103 (2021).
- [12] A. Groisman and V. Steinberg, Elastic turbulence in curvilinear flows of polymer solutions, *New J. Phys.* **6**, 29 (2004).
- [13] E. S. G. Shaqfeh, Purely elastic instabilities in viscometric flows, *Annu. Rev. Fluid Mech.* **28**, 129 (1996).
- [14] G. H. McKinley, P. Pakdel, and A. Oeztekin, Rheological and geometric scaling of purely elastic flow instabilities, *J. Non-Newtonian Fluid Mech.* **67**, 19 (1996).
- [15] P. Pakdel and G. H. McKinley, Elastic Instability and Curved Streamlines, *Phys. Rev. Lett.* **77**, 2459 (1996).
- [16] C. Schäfer, A. Morozov, and C. Wagner, Geometric scaling of elastic instabilities in the Taylor-Couette geometry: A theoretical, experimental and numerical study, *J. Non-Newtonian Fluid Mech.* **259**, 78 (2018).
- [17] R. Benzi and E. S. Ching, Polymers in fluid flows, *Annu. Rev. Condens. Matter Phys.* **9**, 163 (2018).
- [18] E. S. Shaqfeh and B. Khomami, The Oldroyd-B fluid in elastic instabilities, turbulence and particle suspensions, *J. Non-Newtonian Fluid Mech.* **298**, 104672 (2021).
- [19] R. G. Larson, E. S. G. Shaqfeh, and S. J. Muller, A purely elastic instability in Taylor-Couette flow, *J. Fluid Mech.* **218**, 573 (1990).
- [20] E. S. G. Shaqfeh, S. J. Muller, and R. G. Larson, The effects of gap width and dilute solution properties on the viscoelastic Taylor-Couette instability, *J. Fluid Mech.* **235**, 285 (1992).
- [21] S. J. Muller, Elastically-influenced instabilities in Taylor-Couette and other flows with curved streamlines: A review, *Korea-Australia Rheol. J* **20**, 117 (2008).
- [22] C. S. Dutcher and S. J. Muller, Effects of weak elasticity on the stability of high Reynolds number co- and counter-rotating Taylor-Couette flows, *J. Rheol. (Melville, NY, US)* **55**, 1271 (2011).
- [23] N. Latrache, O. Crumeyrolle, and I. Mutabazi, Transition to turbulence in a flow of a shear-thinning viscoelastic solution in a Taylor-Couette cell, *Phys. Rev. E* **86**, 056305 (2012).
- [24] C. S. Dutcher and S. J. Muller, Effects of moderate elasticity on the stability of co- and counter-rotating Taylor-Couette flows, *J. Rheol. (Melville, NY, US)* **57**, 791 (2013).
- [25] M. Avgousti and A. N. Beris, Non-axisymmetric modes in the viscoelastic Taylor-Couette flow, *J. Non-Newtonian Fluid Mech.* **50**, 225 (1993).
- [26] R. Sureshkumar, A. N. Beris, and M. Avgousti, Non-axisymmetric subcritical bifurcations in viscoelastic Taylor-Couette flow, *Proc. R. Soc. London, Ser. A* **447**, 135 (1994).
- [27] M. Renardy, Y. Renardy, R. Sureshkumar, and A. N. Beris, Hopf-Hopf and steady-Hopf interactions in Taylor-Couette flow of an upper-convected fluid, *J. Non-Newtonian Fluid Mech.* **63**, 1 (1996).
- [28] A. Groisman and V. Steinberg, Couette-Taylor Flow in a Dilute Polymer Solution, *Phys. Rev. Lett.* **77**, 1480 (1996).
- [29] A. Groisman and V. Steinberg, Solitary Vortex Pairs in Viscoelastic Couette Flow, *Phys. Rev. Lett.* **78**, 1460 (1997).
- [30] A. Fouxon and V. Lebedev, Spectra of turbulence in dilute polymer solutions, *Phys. Fluids* **15**, 2060 (2003).
- [31] B. Qin and P. E. Arratia, Characterizing elastic turbulence in channel flows at low Reynolds number, *Phys. Rev. Fluids* **2**, 083302 (2017).
- [32] V. Steinberg, Scaling Relations in Elastic Turbulence, *Phys. Rev. Lett.* **123**, 234501 (2019).
- [33] A. Varshney and V. Steinberg, Elastic Alfvén waves in elastic turbulence, *Nat. Commun.* **10**, 652 (2019).
- [34] R. van Buel, C. Schaaf, and H. Stark, Elastic turbulence in two-dimensional Taylor-Couette flows, *Europhys. Lett.* **124**, 14001 (2018).
- [35] K. K. Talwar, H. K. Ganpule, and B. Khomami, A note on selection of spaces in computation of viscoelastic flows using the *hp*-finite element method, *J. Non-Newtonian Fluid Mech.* **52**, 293 (1994).

- [36] B. Yang and B. Khomami, Simulations of sedimentation of a sphere in a viscoelastic fluid using molecular based constitutive models, *J. Non-Newtonian Fluid Mech.* **82**, 429 (1999).
- [37] M. A. Alves, P. J. Oliveira, and F. T. Pinho, Numerical methods for viscoelastic fluid flows, *Annu. Rev. Fluid Mech.* **53**, 509 (2021).
- [38] R. G. Larson and P. S. Desai, Modeling the rheology of polymer melts and solutions, *Annu. Rev. Fluid Mech.* **47**, 47 (2015).
- [39] L. Zhu and L. Xi, Inertia-driven and elastoinertial viscoelastic turbulent channel flow simulated with a hybrid pseudo-spectral/finite-difference numerical scheme, *J. Non-Newtonian Fluid Mech.* **286**, 104410 (2020).
- [40] B. Yu and Y. Kawaguchi, Direct numerical simulation of viscoelastic drag-reducing flow: A faithful finite difference method, *J. Non-Newtonian Fluid Mech.* **116**, 431 (2004).
- [41] K. D. Housiadas and A. N. Beris, An efficient fully implicit spectral scheme for DNS of turbulent viscoelastic channel flow, *J. Non-Newtonian Fluid Mech.* **122**, 243 (2004).
- [42] C. F. Li, R. Sureshkumar and B. Khomami, Influence of rheological parameters on polymer induced turbulent drag reduction, *J. Non-Newtonian Fluid Mech.* **140**, 23 (2006).
- [43] C. F. Li, R. Sureshkumar, and B. Khomami, Simple framework for understanding the universality of the maximum drag reduction asymptote in turbulent flow of polymer solutions, *Phys. Rev. E* **92**, 043014 (2015).
- [44] T. Vaithianathan and L. R. Collins, Numerical approach to simulating turbulent flow of a viscoelastic polymer solution, *J. Comput. Phys.* **187**, 1 (2003).
- [45] Y. Dubief, C. M. W. V. E. Terrapon, E. S. G. Shaqfeh, P. Moin, and S. K. Lele, New answers on the interaction between polymers and vortices in turbulent flows, *Flow, Turbul. Combust.* **74**, 311 (2005).
- [46] J. Song, F. Lin, N. Liu, X. Lu, and B. Khomami, Direct numerical simulation of inertio-elastic turbulent Taylor-Couette flow, *J. Fluid Mech.* **926**, A37 (2021).
- [47] P. Perlekar, D. Mitra, and R. Pandit, Manifestations of Drag Reduction by Polymer Additives in Decaying, Homogeneous, Isotropic Turbulence, *Phys. Rev. Lett.* **97**, 264501 (2006).
- [48] P. Perlekar, D. Mitra, and R. Pandit, Direct numerical simulations of statistically steady, homogeneous, isotropic fluid turbulence with polymer additives, *Phys. Rev. E* **82**, 066313 (2010).
- [49] A. Kurganov and E. Tadmor, New high-resolution central schemes for nonlinear conservation laws and convection-diffusion equations, *J. Comput. Phys.* **160**, 241 (2000).
- [50] T. Vaithianathan, A. Robert, J. G. Brasseur, and L. R. Collins, An improved algorithm for simulating three-dimensional, viscoelastic turbulence, *J. Non-Newtonian Fluid Mech.* **140**, 3 (2006).
- [51] J. Song, Z. Wan, N. Liu, X. Lu, and B. Khomami, A reverse transition route from inertial to elasticity-dominated turbulence in viscoelastic Taylor-Couette flow, *J. Fluid Mech.* **927**, A10 (2021).
- [52] N. Liu and B. Khomami, Polymer-Induced Drag Enhancement in Turbulent Taylor-Couette Flows: Direct Numerical Simulations and Mechanistic Insight, *Phys. Rev. Lett.* **111**, 114501 (2013).
- [53] D. G. Thomas, B. Khomami, and R. Sureshkumar, Nonlinear dynamics of viscoelastic Taylor-Couette flow: Effect of elasticity on pattern selection, molecular conformation and drag, *J. Fluid Mech.* **620**, 353 (2009).
- [54] R. van Buel and H. Stark, Characterizing elastic turbulence in the three-dimensional von Kármán swirling flow using the Oldroyd-B model, *Phys. Fluids* **34**, 043112 (2022).
- [55] R. Sureshkumar, A. N. Beris, and M. Avgousti, Effect of artificial stress diffusivity on the stability of numerical calculations and the dynamics of time-dependent viscoelastic flows, *J. Non-Newtonian Fluid Mech.* **60**, 53 (1995).
- [56] R. Sureshkumar, A. N. Beris, and M. Avgousti, Direct numerical simulation of the turbulent channel flow of a polymer solution, *Phys. Fluids* **9**, 743 (1997).
- [57] A. Groisman and V. Steinberg, Mechanism of elastic instability in Couette flow of polymer solutions: Experiment, *Phys. Fluids* **10**, 2451 (1998).
- [58] J. Song, H. Teng, N. Liu, H. Ding, X. Lu, and B. Khomami, The correspondence between drag enhancement and vortical structures in turbulent Taylor-Couette flows with polymer additives: A study of curvature dependence, *J. Fluid Mech.* **881**, 602 (2019).

- [59] T. Wei, E. M. Kline, S. H. Lee, and S. Woodruff, Görtler vortex formation at the inner cylinder in Taylor-Couette flow, *J. Fluid Mech.* **245**, 47 (1992).
- [60] D. G. Thomas, R. Sureshkumar, and B. Khomami, Pattern Formation in Taylor-Couette Flow of Dilute Polymer Solutions: Dynamical Simulations and Mechanism, *Phys. Rev. Lett.* **97**, 054501 (2006).
- [61] B. Qin, P. F. Salipante, S. D. Hudson, and P. E. Arratia, Upstream vortex and elastic wave in the viscoelastic flow around a confined cylinder, *J. Fluid Mech.* **864**, R2 (2019).
- [62] N. S. Liu and B. Khomami, Elastically induced turbulence in Taylor-Couette flow: Direct numerical simulation and mechanistic insight, *J. Fluid Mech.* **737**, R4 (2013).
- [63] V. Dallas, J. C. Vassilicos, and G. F. Hewitt, Strong polymer-turbulence interactions in viscoelastic turbulent channel flow, *Phys. Rev. E* **82**, 066303 (2010).
- [64] J. Song, N. Liu, X. Lu, and B. Khomami, Direct numerical simulation of elastic turbulence in the Taylor-Couette flow: Transition pathway and mechanistic insight, *J. Fluid Mech.* **949**, A49 (2022).